Is there a difference between T- and B-lymphocyte morphology?

Dmitry I. Strokotov
Maxim A. Yurkin
Konstantin V. Gilev
Institute of Chemical Kinetics and Combustion
Siberian Branch RAS
Institutskaya 3
Novosibirsk, 630090, Russia
    and
Novosibirsk State University
Pirogova 2
Novosibirsk, 630090, Russia

Dirk R. van Bockstaele
Esoterix
Clinical Trials Services
Division of LabCorp
Gen. De Wittelaan L11-A2
Mechelen, B-2800, Belgium

Alfons G. Hoekstra
University of Amsterdam
Faculty of Science
Science Park 107
Amsterdam, 1098 XG, Netherlands

Nikolay B. Rubtsov
Institute of Cytology and Genetics
Siberian Branch RAS
Lavrentyeva 10
Novosibirsk, 630090, Russia

Valeri P. Maltsev
Institute of Chemical Kinetics and Combustion
Siberian Branch RAS
Institutskaya 3
Novosibirsk, 630090, Russia
    and
Novosibirsk State University
Pirogova 2
Novosibirsk, 630090, Russia

Abstract. We characterize T- and B-lymphocytes from several donors, determining cell diameter, ratio of nucleus to cell diameter, and refractive index of the nucleus and cytoplasm for each individual cell. We measure light-scattering profiles with a scanning flow cytometer and invert the signals using a coated sphere as an optical model of the cell and by relying on a global optimization technique. The main difference in morphology of T- and B-lymphocytes is found to be the larger mean diameters of the latter. However, the difference is smaller than the natural biological variability of a single cell. We propose nuclear inhomogeneity as a possible reason for the deviation of measured light-scattering profiles from real lymphocytes from those obtained from the coated sphere model. © *2009 Society of Photo-Optical Instrumentation Engineers.* [DOI: 10.1117/1.3275471]

1 Introduction

Mononuclear cells, lymphocytes, and monocytes form an important part of blood leukocytes.[1] Lymphocytes constitute about 20 to 30% of leukocytes. Approximately one third of all lymphocytes have a lifespan of 10 to 20 days, whereas the remainder can live from hundreds of days to many years. B-lymphocytes take part in antibody production, whereas T-lymphocytes are the mediators of cellular immunity (cytotoxic T-cell responses, delayed-type hypersensitivity, graft-versus-host reactions, and so forth).

Over the last few decades substantial progress has been achieved in flow cytometry immunophenotyping procedures.[2] Nevertheless, morphological analysis and automatic cell sizing remain one of the key points in studying, diagnosing, and classifying lymphoproliferative disorders.[3,4] It is well known that the average size of lymphocytes decreases and density changes (generally increasing) in leukemia.[5,6] The cytoplasmic refractive index of circulating lymphocytes remains invariant among normal human individuals and is elevated for patients bearing malignant tumors.[7] This refractive index also increases significantly in active rheumatoid arthritis, in the immune reaction to a kidney transplant, and pregnancy, especially during the 10 days preceding parturition.

Address all correspondence to: Valeri P. Malsev, Institute of Chemical Kinetics and Combustion, Siberian Branch RAS Institutskaya 3, Novosibirsk, 630090 Russia. Tel: 738-333-33240; Fax: 738-333-07350; E-mail: maltsev@kinetics.nsc.ru

Modern commercial cell counters[8–12] have reached their limit of analytical potential in cell identification and have a weak performance in cell characterization, i.e., in determination of physical characteristics of cells. In particular, blood platelet volume and refractive index, red blood cell volume, and hemoglobin concentration are the only physical characteristics that can be measured reliably with automatic hematology analyzers. Cellular and nuclear size of mononuclear leucocytes and densities of their cytoplasm and nucleus are still out of scope of routine hematological analysis.

Over the last decade we have, however, developed an advanced flow cytometer that is capable of acquiring more physical characteristics of individual particles[13] by measuring detailed light scattering profiles and inverting them by relying on dedicated optical models.[14] In this work we demonstrate the applicability of this scanning flow cytometry to mononuclear cells and apply it to a detailed analysis of the morphology and optical properties of human B- and T-lymphocytes.

A complex angular light-scattering pattern is formed by the interaction of a cell and a laser beam. This pattern is rather sensitive to cell morphology, in particular to the cell size and nucleus shape and displacement for lymphocytes.[15] This sensitivity offers the opportunity to determine individual cell characteristics from a solution of the inverse light-scattering problem. Unfortunately, the inverse light-scattering problem has been solved only for a few shapes and structures of individual particles, namely homogeneous spheres,[13,16–20] prolate spheroids in a fixed orientation,[13] coated spheres (determining only diameters[13] and reference therein), and biconcave disks.[21] Mathematical optimization is a common approach in the solution of inverse problems. This approach utilizes an iterative procedure with multiple evaluations of the direct problem and can be effectively applied, for instance, for characterization of a spherical particle using Mie theory as a solution of the direct light-scattering problem. Neukammer et al.[22] used a flow cytometer together with an intensified charge-coupled device (ICCD) camera to record 2-D patterns of the light scattered by single lymphocytes. Experimental data were fitted with simulations of light scattering from homogeneous spheres with fixed refractive indexes. The refractive index was taken from a typical value of cytoplasm (1.37), and the mean diameter of lymphocytes as estimated by these authors was found to be ~ 7.6 μm.

In a previous paper, we described the measurement of light scattering of human mononuclear blood cells, and proposed an appropriate optical model and a solution of the inverse light-scattering problem for those cells.[23] A multilayered sphere was tested as an optical model for mononuclear blood cells, and a five-layer model gave the best agreement between experimental and theoretical light-scattering profiles (LSP). The inverse light-scattering problem was solved with an optimization procedure based on a multistart Levenberg-Marquardt algorithm. However, the five-layer model of mononuclear cells has a few disadvantages. First, as the model has ten free parameters (five radii and five refractive indices for the corresponding layers), the search space is quite complex and it is hard to guarantee finding the global minimum. Although it was empirically proven that as many as 2500 restarts of the optimization procedure resulted in a reliable global minimum, such testing of robustness consumes a lot of computational time (about one hour per cell). Second, and more important, that method did not provide (statistically reliable) errors of estimates of characteristics of individual cells, which is crucial to assess the overall adequacy of the fitting procedure.

In this work we construct a solution of the inverse light-scattering problem for mononuclear cells, modeled as a coated sphere. The theory of light scattering by a sphere consisting of two layers is well known,[24] and light-scattering profiles are easily and quickly computed. To perform global optimization, we use the algorithm DIRECT (an acronym for DIviding RECTangles)[25] and propose a method to compute errors of the estimated cellular characteristics. We measured absolute differential cross sections and determined distributions over cell characteristics (nucleus and cell sizes and refractive indices) for samples of T-lymphocytes of seven donors and samples of B-lymphocytes of two donors. For that we develop a method to characterize the sample based on individual measurements with different errors. We also compared morphological characteristics of T- and B-lymphocytes of the same donors.

2 Materials and Methods

2.1 Sample Preparation

Blood samples were taken from healthy donors by venopuncture with EDTA as an anticoagulant. Preparation of lymphocyte samples was carried out by a density-gradient separation procedure.[26] This procedure consists of diluting 2 ml of whole anticoagulated blood in 6 ml of phosphate buffered saline (PBS) and centrifuging at ≈ 450 g for 20 min through a Ficoll®-sodium metrizoate solution with a density of 1.077 g/ml. Then a thin layer of mononuclear cells from the plasma/Ficoll interface was aspirated, washed with PBS in a centrifuge, and stained with immunofluorescence markers CD3-FITC and CD19-PE (ImmunoTools, Friesoythe, Germany) for T- and B-lymphocytes, respectively. After 20 min of staining, the sample was washed again and diluted to a concentration of about 10^6 cells/ml. The prepared samples were analyzed with a scanning flow cytometer (SFC) measuring the LSPs and fluorescence signals from each cell. Clusters containing all lymphocytes were gated by light-scattering signals. In conventional flow cytometry, identification of lymphocytes can be performed using forward and side scattering, with intensities plotted on the well-known "side scattering versus forward scattering" (SSC×FSC) map. Analogously, in SFC we used absolute values of the integrated whole light-scattering trace instead of the side scattering [Fig. 1(a)]. Dot plots of these two integral parameters were verified to be similar to and display the same population percentages as ones obtained by the standard flow cytometer Coulter Epics (Beckman Coulter, Fullerton, California) (data not shown). Then T- and B-lymphocytes subsets from this cluster were distinguished by specific fluorescence using the CD3 ×CD19 map [Fig. 1(b)].

2.2 Scanning Flow Cytometer and Confocal Microscopy

The schematic layout of the SFC's optical system is presented in Fig. 2. The SFC was assembled on the bench of a FACStar
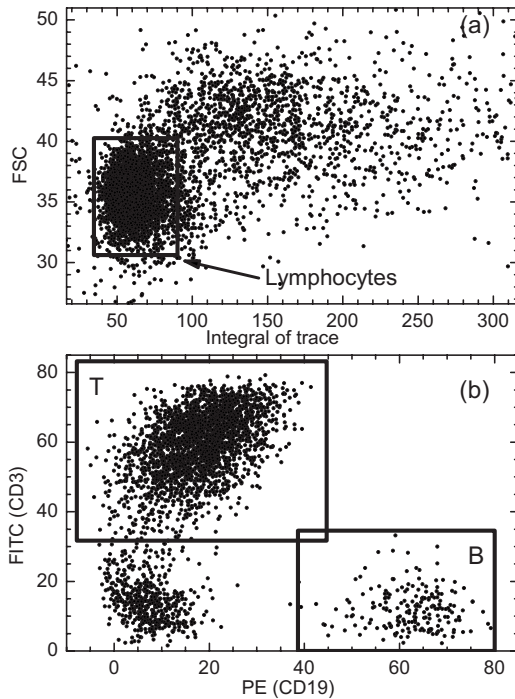
Fig. 1 2-D cytograms used in identification of T- and B-cells.

Plus BD flow cytometer (BD, Franklin, Lakes, New Jersey). An argon-ion laser (laser, 488 nm, 60 mW) was used for generation of the scattering pattern, for excitation of fluorescence, and for triggering the electronic unit. The laser beam split by mirror 1 is directed coaxially with the stream by mirrors 2 and 3, and a lens (lens 1, $f=45$ mm) through a hole in the mirror (mirror 4). The hydrofocusing head (not shown) produces two concentric fluid streams: a sheath stream without particles and a probe stream that carries the particles. The fluidics system directs a probe stream with a 12 μm diam into the optical cell (Fig. 2). The operational function of the optical cell was previously described in detail.[13,27] The light scattered by a single cell is reflected by mirror 4 to the photomultiplier tube (PMT 2). The other portion of the laser beam is focused by objective
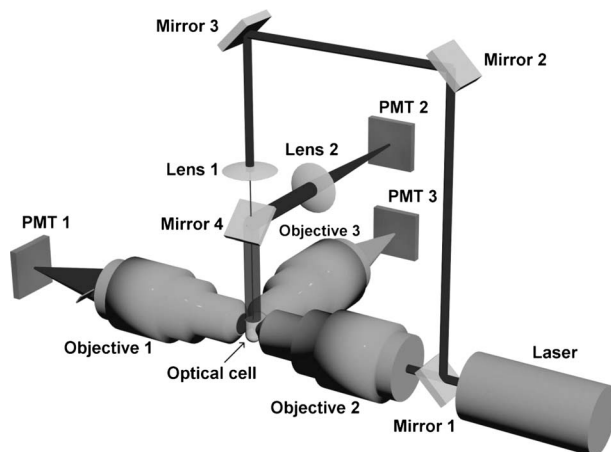

Fig. 2 Schematic layout of the optical system of the scanning flow cytometer.

2 (NA=0.2) into the capillary of the optical cell. The light scattered in the forward direction is collected by objective 1 (NA=0.2) and detected by PMT 1. The beam stop prevents illumination of PMT 1 by the incoming laser beam. The fluorescence of specific dye molecules linked at the single cell is collected by objective 3 (NA=0.4) and detected by PMT 3. The bandpass optical filter provides measurement of the specific fluorescence with an appropriate signal-to-noise ratio.

This optical setup of the SFC (PMT 2 in Fig. 2) measures the following combination of scattering matrix elements:[13]

$$I(\theta) = \frac{1}{2\pi} \int_0^{2\pi} [S_{11}(\theta,\varphi) + S_{12}(\theta,\varphi)\cos(2\varphi) \\ - S_{13}(\theta,\varphi)\sin(2\varphi)]d\varphi, \quad (1)$$

where S_{ij} are the elements of the Mueller matrix, and θ and φ are polar and azimuth scattering angles, respectively. For spherically symmetric scatterer, Eq. (1) becomes:[21]

$$I(\theta) = \frac{1}{2\pi} \int_0^{2\pi} S_{11}(\theta,\varphi)d\varphi. \quad (2)$$

In general, experimental data have a different signal-to-noise ratio over regions measured that assume a multiplication of theoretical data with a weighting function to reduce an effect of the noise on the fitting results. In the current study we propose

$$w(\theta) = \frac{1 \deg}{\theta} \exp[-2\ln^2(\theta/54 \deg)], \quad (3)$$

which is an approximate description of the normalizing coefficient of the SFC transfer function[13] by a log-normal function.

The operation angular range of the SFC is limited by geometrical parameters of the optical cell and alignment of the laser beam. We determined the operation range from analysis of polymer microspheres. The angular range, where experimental weighted LSP $w(\theta)I(\theta)$ is perfectly fitted by weighted LSP calculated from Mie theory, constitutes the operational range of the SFC for measurement of the light-scattering properties of blood cells. The result of a representative result is shown in Fig. 3, where the inset shows the measured light-scattering trace of a single microsphere. Note that for microspheres in the size range of 0.5 to 10 μm and refractive index range of 1.56 to 1.59, such excellent results are obtained routinely with SFC.[13] The comparison of experimental and theoretical weighted LSPs allows us to set the operation region of the current SFC setup to the range from 12 to 50 deg.

A Carl Zeiss LSM 510 META confocal microscope was used to develop our optical model of lymphocytes. The typical parameters of the microscopy used in this work were as follows: objective—Plan-Apochromat 100×1.4 Oil DIC; wavelength—543 nm and 405 nm; filters—BP 560–615 nm and LP 420 nm; scaling—30 nm $(\Delta x, \Delta y, \Delta z)$.

2.3 Discrete Dipole Approximation

The discrete dipole approximation (DDA) is a general method to compute scattering and absorption of electromagnetic
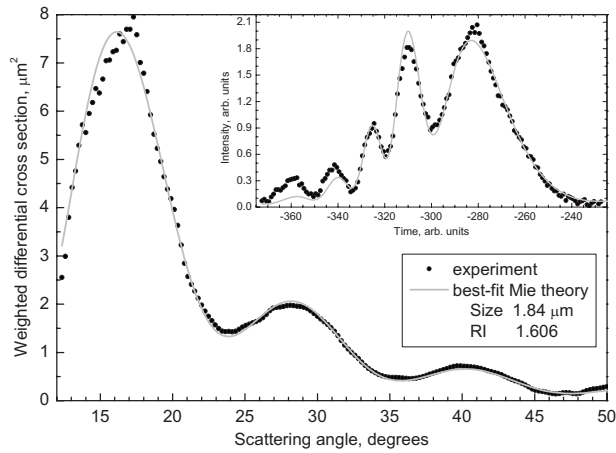
Fig. 3 Experimental and Mie theory best-fit weighted differential cross sections of an individual polymer microsphere. The Mie result corresponds to a microsphere with a size of 1.84 μm and refractive index of 1.606. The measured light-scattering trace of the same microsphere is shown in the inset.
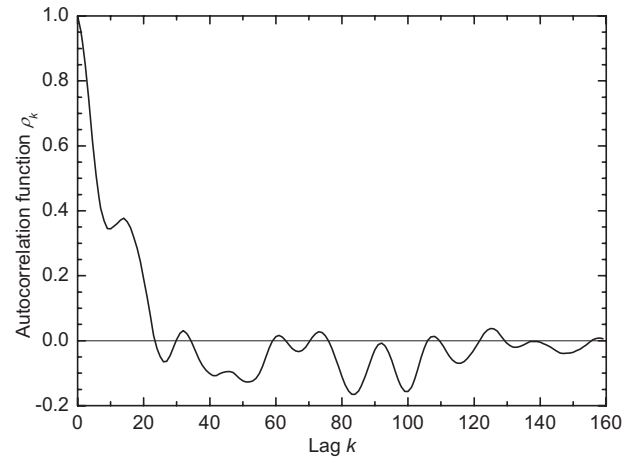

Fig. 4 Typical autocorrelation function of residuals, resulting from fitting of a lymphocyte LSP by LSPs calculated from the Mie theory for coated spheres.

waves by particles of arbitrary geometry and composition.[28] The ADDA computer code is an efficient DDA implementation on a cluster of computers, parallelizing a *single* DDA computation;[29] ADDA's source code and documentation is freely available.[30] Simulations of light scattering by the nonsymmetric optical model of a lymphocyte (see Sec. 3.2) were performed with ADDA v.0.78.2. For each particle, we computed the LSP [see Eq. (1)] for θ from 12 to 50 deg with steps of 0.5 deg, using steps of 5.6 deg for integration over φ. All simulations were run on the Dutch compute cluster Lisa.[31]

2.4 Global Optimization

The solution of the inverse problem is performed by a least-squares method, i.e., by minimizing the weighted sum of squares:

$$S(\boldsymbol{\beta}) = \sum_{i=1}^{N} z_i^2, \quad z_i = w(\theta_i)[I_{\text{th}}(\theta_i, \boldsymbol{\beta}) - I_{\text{exp}}(\theta_i)], \quad (4)$$

where $\boldsymbol{\beta}$ is a vector of p model parameters, and I_{th} and I_{exp} are theoretical and experimental LSP, respectively. In this work we use $N=160$ (in the range of θ from 12 to 50 deg) and $p=4$ (described later). For lymphocytes, the LSP calculated from Eq. (2) has a strong oscillating structure, and hence, the function $S(\boldsymbol{\beta})$ possesses multiple local minima (data not shown), which may present problems for straightforward (local) optimization algorithms. To solve this problem, we use the DIRECT algorithm,[25] which performs an extensive search over the parameter space, described by a 4-D rectangular parallelepiped **B**, requiring a lot of computational time (a few minutes per lymphocyte). However, in addition to finding the global minimum of $S(\boldsymbol{\beta})$, i.e., the best estimate $\boldsymbol{\beta}_0$, it provides an approximate description of the whole least-square surface, which we further use to estimate the parameter errors.

We use the following cellular characteristics: cell diameter D_c, ratio of nucleus and cell diameters D_n/D_c, refractive indices of cytoplasm m_c, and nucleus m_n. The region **B** is defined by their boundary values: $D_c \in [4.5, 10]$ μm,

$D_n/D_c \in [0.7, 0.95]$, $m_c \in [1.34, 1.41]$, and $m_n \in [1.41, 1.58]$, excessively covering the range of lymphocyte morphological characteristics as reported in recent literature.[7,32–34]

2.5 Errors of Parameter Estimates

Many textbooks on nonlinear regression deal with errors of parameter estimates (see e.g., Refs. 35 and 36). However, most of the theory is worked out for the case of normally distributed and independent experimental errors. Unfortunately, there is significant dependence between residuals z_i in our case, which can be characterized by a sample autocorrelation function ρ_k.[35] A typical example of this function for a lymphocyte is shown in Fig. 4. The correlation is caused by: 1. finite angular resolution of the SFC, causing dependence between nearby θ_i, and 2. model errors, i.e., systematic difference between lymphocyte shape and a coated sphere (see Sec. 3.2). The correlation due to angular resolution (about 0.5 deg[13]) may extent only up to approximately $k=3$; therefore, a major cause for correlation is model errors. These errors are definitely not purely random, but they are determined by a number of parameters, such as, e.g., an offset of nucleus from the cell center or its inhomogeneity, which have large biological variability in the sample and hence can be considered random for any particular lymphocyte. There are also certain errors associated with imperfect alignment of SFC and noncentral positions of the particle in the flow.[13] However, we consider these errors as part of model errors, since the exact structure and cause of the latter is not important for our characterization method, nor can they be distinguished from real model errors.

Rigorous methods to deal with correlated residuals exist,[35] but they are quite cumbersome. Here we propose to use an approximate but much simpler approach. It is known[37] that the sum of squares of correlated residuals can be approximately described by a χ^2 distribution, if correlations can be described by a stationary Gaussian process, i.e., if it is fully characterized by ρ_k. The number of effective degrees of freedom of the resulting χ^2 distribution is

$$n = \frac{N^2}{N + 2\sum_{k=1}^{N-1} (N-k)\rho_k^2}. \tag{5}$$

Intuitively, one may think of n as N divided by the decay length of ρ_k. We assume that for the purpose of statistical inference, our N correlated residuals are equivalent to n independent residuals. Although this is certainly an approximation, it satisfies the limiting values: fully independent residuals $\rightarrow n = N$, fully dependent $\rightarrow n = 1$. Moreover, this approach tracks the main effect of residual correlations—larger probability of large sum of squares, and hence, wider confidence regions. We determine n for each lymphocyte; its typical distribution over a sample is shown in Fig. 5.

Next, we apply a Bayesian inference method with standard noninformative (or homogeneous) prior $P(\sigma, \boldsymbol{\beta}) \sim \sigma^{-1}$.[35] The posterior probability density of $\boldsymbol{\beta}$ given a specific experimental LSP is then $P(\boldsymbol{\beta}|I_{\exp}) = \kappa[S(\boldsymbol{\beta})]^{-n/2}$, where κ is a normalization constant obtained as

$$\kappa = \left(\int_{\mathbf{B}} [S(\boldsymbol{\beta})]^{-n/2} d\boldsymbol{\beta} \right)^{-1}. \tag{6}$$

To calculate integrals involving $[S(\boldsymbol{\beta})]^{-n/2}$ over $\mathbf{B}$, we use the output of the DIRECT algorithm—a partition of $\mathbf{B}$ into $M(\sim 10^4)$ parts with volumes V_i and centers $\boldsymbol{\beta}_i$, with values $S_i = S(\boldsymbol{\beta}_i)$ also known. Since this partition is fine where S is small and coarse where S is large (due to the internal structure of DIRECT[25]), such integrals can be approximated by a sum with good accuracy. This is used to calculate averages of any quantity $f(\boldsymbol{\beta})$:

$$\langle f(\boldsymbol{\beta}) \rangle = \kappa \int_{\mathbf{B}} f(\boldsymbol{\beta})[S(\boldsymbol{\beta})]^{-n/2} d\boldsymbol{\beta} = \kappa \sum_{i=1}^{M} f(\boldsymbol{\beta}_i) S_i^{-n/2} V_i,$$

$$\kappa = \left(\sum_{i=1}^{M} S_i^{-n/2} V_i \right)^{-1}. \tag{7}$$

Since we know the complete probability distribution of model parameters for any measured particle, we can infer any statistical characteristics of this distribution. In this work, we calculate the expectation value $\boldsymbol{\mu} = \langle \boldsymbol{\beta} \rangle$ and the covariance matrix $\mathbf{C} = \langle (\boldsymbol{\beta} - \boldsymbol{\mu})(\boldsymbol{\beta} - \boldsymbol{\mu})^T \rangle$ using Eq. (7), since in most cases the probability distribution is well described by a multidimensional normal distribution (data not shown). Other quantities of interest are the highest posterior density (HPD) confidence regions, defined as $\mathbf{B}_{\mathrm{HPD}}(P_0) = \{\boldsymbol{\beta} | P(\boldsymbol{\beta} | I_{\exp}) > P_0\}$.[35] Its confidence level is

$$\alpha = \kappa \int_{\mathbf{B}_{\mathrm{HPD}}(P_0)} [S(\boldsymbol{\beta})]^{-n/2} d\boldsymbol{\beta}. \tag{8}$$

We use these confidence regions to assess the influence of parameter space boundaries on the results. Although $\mathbf{B}$ is quite large, its boundaries cut off tails of the distribution, causing bias in determination of both $\boldsymbol{\mu}$ and $\mathbf{C}$. The bias increase with relative weight of the cut tail, so we define a confidence level α of the particle (more precisely, of associated probability distribution over $\boldsymbol{\beta}$) as the confidence level of
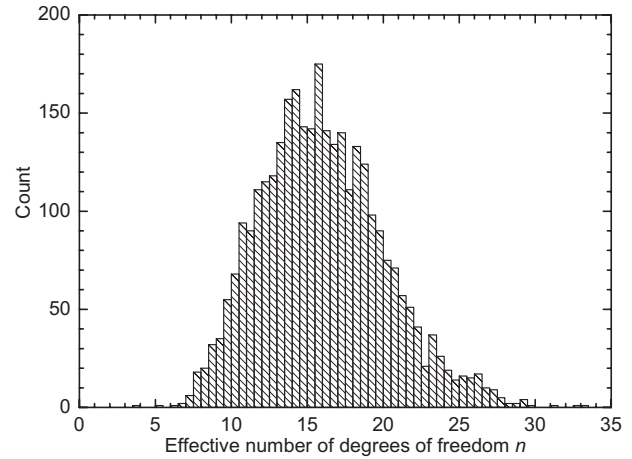

Fig. 5 Distribution of effective number of degrees of freedom over a sample of T-lymphocytes from donor 6.

the HPD region touching the boundary of $\mathbf{B}$. It is important to note that in 4-D parameter space, $1 - \alpha$ is much larger then the weight of the tail cut by the boundary. Therefore, choosing, e.g., $\alpha = 0.8$ implies a small bias of $\boldsymbol{\mu}$ and $\mathbf{C}$.

The main purpose of α is to assess biases of $\boldsymbol{\mu}$ and $\mathbf{C}$. It can also be used as a measure of goodness of fit but only approximately, because it depends on the position of $\boldsymbol{\mu}$ relative to the boundary of $\mathbf{B}$. Relative goodness of fit is better assessed by the matrix $\mathbf{C}$.

2.6 Sample Characterization

Having determined characteristics of each lymphocyte with certain errors (i.e., $\boldsymbol{\mu}_i$ and $\mathbf{C}_i$, $i = 1, \dots, N_s$, where N_s is the number of cells analyzed), we propose the following method to estimate population mean and variances. General normal distributions are assumed for both the measurement results of individual particles and the true distribution of characteristics over a sample, the latter being described by a mean value $\mathbf{h}$ and covariance matrix $\mathbf{A}$. We use an estimator proposed by Fuller,[38] whose first step is based on means of $\boldsymbol{\mu}_i$ and $\mathbf{C}_i$ and a sample covariance matrix based on $\boldsymbol{\mu}_i$:

$$\bar{\boldsymbol{\mu}} = \frac{1}{n} \sum_i \boldsymbol{\mu}_i, \quad \bar{\mathbf{C}} = \frac{1}{n} \sum_i \mathbf{C}_i,$$

$$\bar{\mathbf{M}} = \frac{1}{n-1} \sum_i (\boldsymbol{\mu}_i - \bar{\boldsymbol{\mu}})(\boldsymbol{\mu}_i - \bar{\boldsymbol{\mu}})^T. \tag{9}$$

$\bar{\mathbf{M}} - \bar{\mathbf{C}}$ is an unbiased estimator of $\mathbf{A}$, but it should be modified to ensure positive semidefiniteness: $\mathbf{A}^{(0)} = \mathbf{F}(\bar{\mathbf{M}}, \bar{\mathbf{C}})$, where the transformation $\mathbf{F}$ is defined as

$$\mathbf{F}(\mathbf{X}, \mathbf{Y}) = \mathbf{X}^{1/2} \mathbf{Q} \mathbf{D}' \mathbf{Q}^T \mathbf{X}^{1/2}, \quad \text{where}$$

$$\mathbf{I} - \mathbf{X}^{-1/2} \mathbf{Y} \mathbf{X}^{-1/2} = \mathbf{Q} \mathbf{D} \mathbf{Q}^T, \quad \mathbf{D}' = \max(0, \mathbf{D}). \tag{10}$$

In other words, $\mathbf{Q}$ and $\mathbf{D}$ are orthogonal and diagonal matrices, respectively, obtained by diagonalizing $\mathbf{I} - \mathbf{X}^{-1/2} \mathbf{Y} \mathbf{X}^{-1/2}$, and $\mathbf{D}'$ is $\mathbf{D}$ with negative values replaced by zeroes (maximum is considered element-wise).

The second step is the following:

$$\mathbf{X}_i = \left[\frac{n-1}{n}(\mathbf{A}^{(0)} + \mathbf{C}_i) + \frac{1}{n}\bar{\mathbf{M}} \right]^{-1}, \quad \mathbf{Z} = \left(\sum_i \mathbf{X}_i \right)^{-1},$$

$$\boldsymbol{\mu}_0 = \mathbf{Z}\sum_i \mathbf{X}_i \boldsymbol{\mu}_i,$$

$$\mathbf{M}_0 = \mathbf{G}(\{\mathbf{X}_i, (\boldsymbol{\mu}_i - \boldsymbol{\mu}_0)(\boldsymbol{\mu}_i - \boldsymbol{\mu}_0)^T\}),$$
$$\mathbf{C}_0 = \mathbf{G}(\{\mathbf{X}_i, \mathbf{C}_i\}), \quad \mathbf{A}^{(1)} = \mathbf{F}(\mathbf{M}_0, \mathbf{C}_0), \qquad (11)$$

where $\mathbf{G}(\{\mathbf{X}_i, \mathbf{Y}_i\})$ is a solution of the matrix equation

$$\sum_i \mathbf{X}_i (\mathbf{Y}_i - \mathbf{G})\mathbf{X}_i = 0, \qquad (12)$$

which is straightforward, e.g., by considering symmetric matrices as vectors of $p(p+1)/2$ elements (ten in our particular case). Fuller[38] proved asymptotic equivalence to maximum likelihood estimators, and noted that the second step may be iterated to further improve the estimator. In this work, we iterate Eq. (11) to convergence. The resulting $\boldsymbol{\mu}_0$ is an estimate for $\mathbf{h}$, whose covariance matrix ("error of mean") is $\mathbf{Z}$,[38] and $\mathbf{A}^{(k)}$ is an estimate of $\mathbf{A}$.

The advantage of this procedure is the automatic decrease of importance of measurements with large errors. Therefore, we can seamlessly include all measurements into the estimation of cell characteristics, even those that seem unreliable due to large sums of squares and/or standard deviations of the characteristics. However, doing so is not the best option because of the bias due to the region boundaries, which are especially important for particles with small confidence level α. We also found that the iterative procedure fails to converge when certain cells with large estimate errors are included in the processed sample (data not shown). In the current study, we excluded such cells—they all had $\alpha < 0.35$ and their total amount was less than 0.7% of all cells in each sample.

Therefore, we consider only particles with $\alpha \geq \alpha_0$ for characterization of the samples. To choose the threshold α_0, we plot the resulting parameter estimates versus α_0. Such a plot for mean cell diameter over sample including errors of mean is shown in Fig. 6, together with the fraction of processed cells (those above the threshold). One can see that there are a number of cells, for which α equals exactly zero. That is because the maximum of the probability distribution is reached at the boundary of the parameter space. With decreasing α_0, the error of mean first decreases due to the increasing number of processed cells (better statistics). Then it stabilizes, however, since new accepted measurements have relatively large errors and hence contribute very little new information. The mean value, on the contrary, shows a systematic trend with decreasing α_0 (at least after a certain value), which is due to the "boundary" biases discussed before. As a compromise, we chose a round value $\alpha_0 = 0.8$ for this work; however, we stress that moderate variation of α_0 does not significantly change the results. Plots for other parameters and samples support this choice (data not shown).

For 4-D normal distributions without correlations, a confidence level of 0.8 corresponds to a distance between mean and boundary equal to roughly 2.5 standard deviations. Using
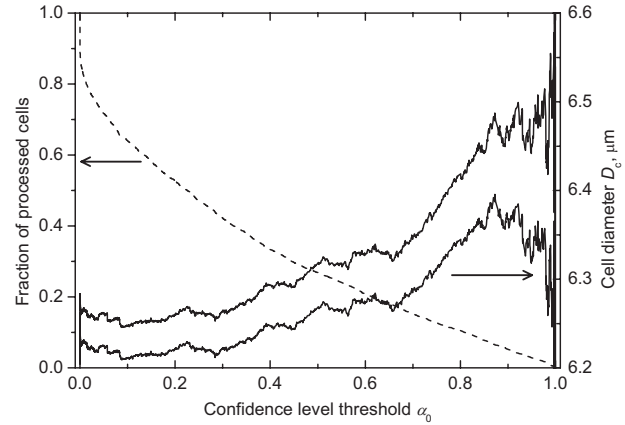

Fig. 6 Dependence of estimated mean cell diameter and fraction of processed cells on confidence level threshold for a sample of T-lymphocytes of donor 6. Confidence interval for $\langle D_c \rangle$ is shown (expected value±standard error). The discontinuity at $\alpha_0 = 0$ is caused by a significant fraction of cells having $\alpha = 0$.

a confidence level threshold does introduce a certain bias, because measurements close to the boundary are less likely to pass the threshold, but we estimate it to be within errors of mean for samples studied in this work. However, it makes sense to broaden the parameter space in future studies to remove such biases altogether, especially when studying samples from nonhealthy donors.

It is important to note that we estimate a full covariance matrix of the sample of individual lymphocytes as well, including correlations between different characteristics. However, we have shown and analyzed only the diagonal elements of the matrices $\mathbf{A}$ and $\mathbf{Z}$, i.e., variances of the characteristics over the sample and errors of mean values. Correlations are significant, e.g., the correlation between D_c and both m_c and m_n are generally between -0.6 and -0.8, but we leave this interesting and potentially biologically significant observation for future study.

3 Results and Discussion

3.1 Differential Light-Scattering Cross Section of Lymphocytes

The essential feature of the SFC is the ability to measure the absolute differential light-scattering cross section of single particles of any shape and structure. This feature is realized by measurement of a mixture of unknown particles and polymer microspheres.[39] The LSP of the polymer microsphere, measured with the SFC, gives a high accuracy agreement with the Mie theory.[40] This allows calibration in absolute light-scattering units. The differential cross section was calculated from the following equation:

$$\frac{d\sigma}{d\theta} = I(\theta)\left(\frac{\lambda}{2\pi m_0} \right)^2, \qquad (13)$$

where I is the LSP from the SFC [Eq. (1)], λ is the wavelength of the incident light, and m_0 is the refractive index of the surrounding medium. In our calculations of the cross section, we used a wavelength of 488 nm and the refractive index of the medium was 1.337.
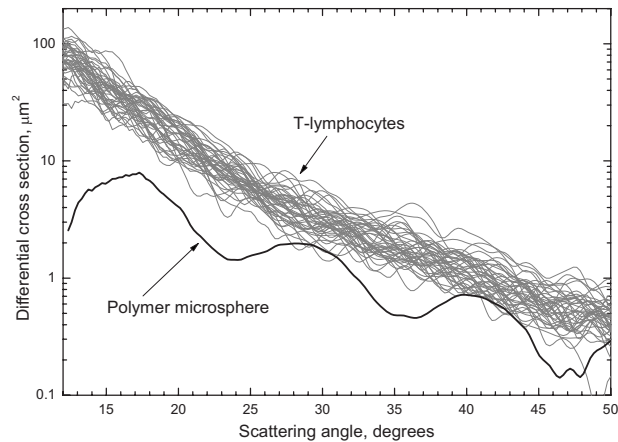
Fig. 7 Differential light-scattering cross section of T-lymphocytes and a polymer microsphere at a wavelength of 488 nm (in logarithmic scale). The polymer microsphere is the same as shown in Fig. 3.

To determine the differential cross section for lymphocytes, we simultaneously analyzed blood leukocytes and polystyrene microspheres with a size of 1.8 μm. 20 LSPs of individual T-lymphocytes and one microsphere are presented in Fig. 7. The experimental LSP of the microsphere, which provides the scale for the y axis of the figure, is the same as shown in Fig. 3. The LSPs of lymphocytes demonstrate substantial variations in their intensity and structure over the sample. Following our analysis of confocal 3-D images of the cells, we suggest that variations in the LSP structure are caused by inhomogeneity and irregular shape of the nucleus.
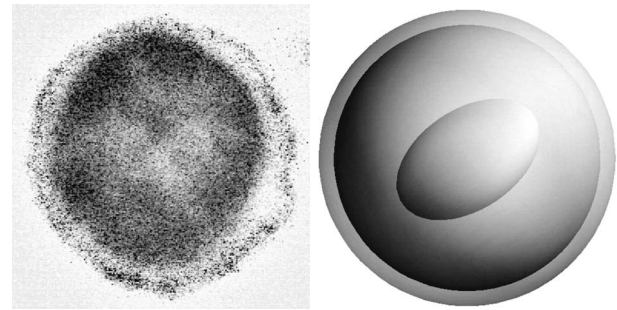

Fig. 8 Slice from the confocal image (left) and (improved) optical model (right) of a lymphocyte.

The variations in the LSP intensity result from differences in effective refractive index of the nucleus and cellular volumes.

3.2 Lymphocyte Optical Model

A lymphocyte has a nearly spherical shape and a single nucleus.[32] 3-D images of a few cells were obtained from confocal microscopy, and one slice of them is presented in the left part of Fig. 8. One can see that the coated sphere is an adequate first-order model, and this model was used for the solution of the inverse light-scattering problem. However, it is also clear that the nucleus is certainly not perfectly homogeneous. To study the effect of such nuclear inhomogeneity on the light scattering, we enhanced the optical model by introducing an oblate spheroid into the nucleus (Fig. 8, right). This model was used to mimic the effect that nuclear inhomogeneity may have on the LSPs and to verify the results of global

Table 1 Results of characterization of T-lymphocytes of seven donors. $\langle . \rangle$, $\sigma(.)$, and $\sigma(\langle . \rangle)$ denote estimated mean, standard deviation, and standard error of mean, respectively.

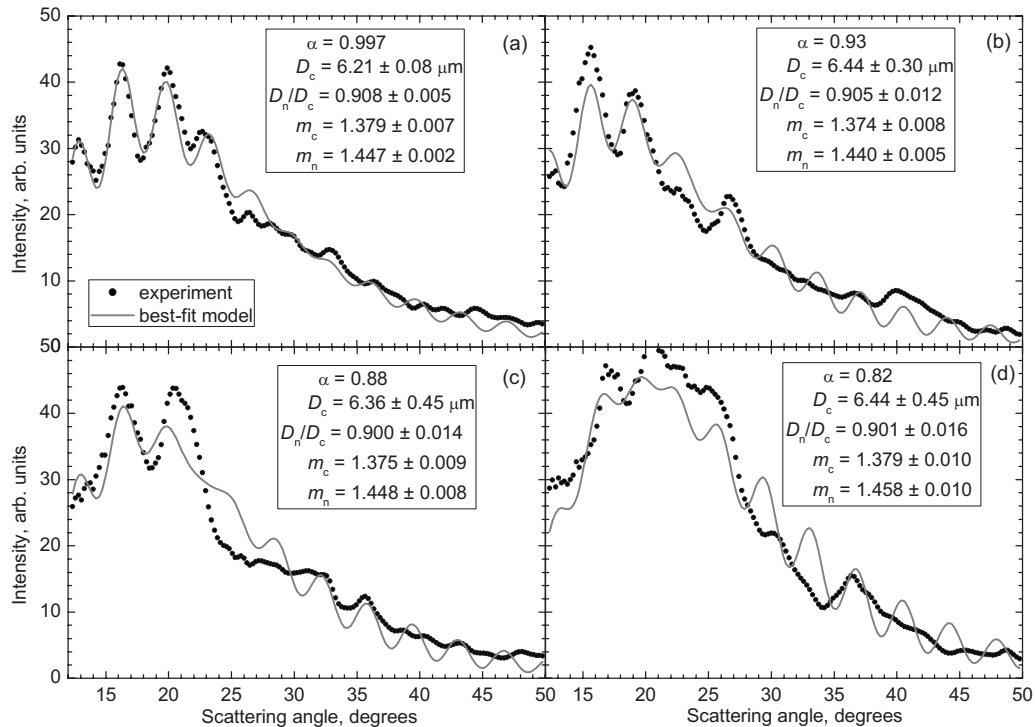|	Donor						
	1	2	3	4	5	6	7
Sample size	225	356	322	243	288	330	205
$\langle D_c \rangle$, μm	6.31	6.36	6.35	6.48	6.34	6.38	6.45
$\sigma(D_c)$, μm	0.50	0.55	0.63	0.60	0.67	0.57	0.71
$\sigma(\langle D_c \rangle)$, μm	0.04	0.03	0.04	0.04	0.04	0.04	0.05
$\langle D_n/D_c \rangle$	0.901	0.901	0.903	0.906	0.903	0.903	0.905
$\sigma(D_n/D_c)$	0.005	0.006	0.007	0.005	0.006	0.005	0.007
$\sigma(\langle D_n/D_c \rangle)$	0.001	0.001	0.001	0.001	0.001	0.001	0.001
$\langle m_c \rangle$	1.3759	1.3755	1.3764	1.3756	1.3774	1.3765	1.3768
$\sigma(m_c)$	0.0026	0.0020	0.0027	0.0030	0.0030	0.0026	0.0030
$\sigma(\langle m_c \rangle)$	0.0005	0.0004	0.0004	0.0005	0.0005	0.0004	0.0006
$\langle m_n \rangle$	1.4479	1.4436	1.4464	1.4411	1.4515	1.4476	1.4486
$\sigma(m_n)$	0.0080	0.0084	0.0086	0.0088	0.0091	0.0080	0.0091
$\sigma(\langle m_n \rangle)$	0.0007	0.0006	0.0006	0.0007	0.0007	0.0006	0.0008

Fig. 9 Results of global optimization for four experimental LSPs of T-lymphocytes from donor 6, showing experimental and best-fit weighted LSPs. The graphs correspond to a different reliability level of the fit α, decreasing from (a) to (d). Estimates of the cell characteristics (expectation value±standard deviation) are also shown.

optimization algorithms in the presence of model errors. We stress once more that our global optimization is based on the simpler coated sphere model, while the more complicated model was only used for a few simulations.

3.3 Characterization of Mononuclear Cells from Light Scattering

We measured leucocytes of seven donors, identifying T- and B-cells using the procedures described in Sec. 2.1. The global optimization algorithm described in Secs. 2.4 and 2.5 was applied to each cell. Results of this procedure for four typical cells from a sample of T-cells of one donor are shown in Fig. 9, together with the confidence level α (see Sec. 2.5). Characterization of the sample is performed according to Sec. 2.6. The ratio of LSPs that passed the confidence level threshold varied from 10 to 20% from sample to sample. The results of characterization are presented in Table 1 (shown sample size is after applying the threshold). We characterized samples of B-cells only for two donors because of the small amount of B-lymphocytes above the threshold for the other donors. Results for these two donors comparing B- and T-lymphocytes are shown in Table 2.

We tested the effect of applying the confidence level threshold by processing all data without it. For illustration, sample parameters related to cell diameter are shown in Table 3. Comparing it with Tables 1 and 2, one can see that for all samples the standard deviation is about 1.5 times larger and the standard error of mean is about two times smaller. This can be explained by the acceptance of values close to the parameter space boundary and larger sample size, respectively. Moreover, the mean value is significantly shifted (es-

Table 2 Comparison of model characteristics of T- and B-lymphocytes of two donors. $\langle.\rangle$, $\sigma(.)$, and $\sigma(\langle.\rangle)$ denote estimated mean, standard deviation, and standard error of mean, respectively. Results for T-lymphocytes duplicate corresponding columns of Table 1.

	Donor 1		Donor 6	
	T	B	T	B
Sample size	225	146	330	86
$\langle D_c \rangle$, μm	6.31	6.63	6.38	6.63
$\sigma(D_c)$, μm	0.50	0.65	0.57	0.73
$\sigma(\langle D_c \rangle)$, μm	0.04	0.06	0.04	0.09
$\langle D_n / D_c \rangle$	0.901	0.904	0.903	0.905
$\sigma(D_n / D_c)$	0.005	0.007	0.005	0.008
$\sigma(\langle D_n / D_c \rangle)$	0.001	0.001	0.001	0.001
$\langle m_c \rangle$	1.3759	1.3766	1.3765	1.3766
$\sigma(m_c)$	0.0026	0.0024	0.0026	0.0027
$\sigma(\langle m_c \rangle)$	0.0005	0.0006	0.0004	0.0008
$\langle m_n \rangle$	1.4479	1.4502	1.4476	1.4490
$\sigma(m_n)$	0.0080	0.0086	0.0080	0.0094
$\sigma(\langle m_n \rangle)$	0.0007	0.0009	0.0006	0.0013

Table 3 Results of characterization of all lymphocyte samples using no confidence level threshold. Only parameters related to cell diameter are shown. These results are expected to be significantly biased by parameter space boundaries.

Donor	T-lymphocytes							B-lymphocytes	
	1	2	3	4	5	6	7	1	6
$\langle D_c \rangle$, μm	6.32	6.27	6.10	6.51	5.83	6.22	6.15	6.67	6.60
$\sigma(D_c)$, μm	0.85	0.79	0.73	0.86	0.74	0.79	0.75	0.92	0.89
$\sigma(\langle D_c \rangle)$, μm	0.02	0.02	0.02	0.02	0.02	0.02	0.02	0.04	0.05

pecially for T-lymphocytes of donors 5 and 7), showing larger variability between different donors. However, as discussed in Sec. 2.6, these results are systematically biased. Therefore, we consider them less reliable and stick to results obtained with confidence level thresholds in further discussions.

The mean values of lymphocyte diameter reported in the literature for normal donors as determined by the Coulter principle were 6.7 μm[41] and 7.3 μm,[42,43] by electron microscopy were 6.5 μm[44] and 5.4 μm,[45] and by optical microscopy a range from 7.68 to 7.88 μm was obtained (for six donors, samples contained 4 to 8% monocytes),[46] from 6 to 8.3 μm (for 12 donors),[32] and from 6.6 to 8.2 μm (for six donors).[33] Standard deviations of D_c are 0.6 μm,[41] from 0.4 to 1.2 μm (12 donors),[32] and from 0.4 to 0.8 μm (six donors),[33] showing no significant difference between different methods. Mean diameter ratios D_n/D_c as determined by electron microscopy were 0.78[44] and 0.56,[45] and as determined by optical microscopy varied from 0.82 to 0.90 (three donors).[32] Data specific to T-lymphocytes are also available for two donors.[32] D_c=7.8 ± 0.7 and 8.3 ± 0.8 μm (mean ± standard deviation), and $\langle D_n/D_c \rangle$=0.80 and 0.85.

To summarize, there is disagreement between different methods, and our results for cell and nucleus diameter fall within the broad range of literature data. However, our data there are unusually small variations in mean size of T-cells and their nucleus from donor to donor (even accounting for error of mean). This fact disagrees with recent microscopic measurements,[32,33] and currently we cannot explain this. There seems to be no reason for our processing algorithm to decrease the natural variability of mean T-cell sizes between the donors, e.g., by somehow concentrating it to 6.4 μm. This is also supported by the fact that mean sizes of B-cells are significantly different. Therefore, we can only hypothesize that either donors studied in this work are more uniform (in age, health condition, etc.) than in previous studies, or the microscopic method together with corresponding sample preparation is susceptible to some measurement errors that increases the visible variability between the donors. For instance, the authors of the optical microscopy study of several donors[32,33] discussed the nonsphericity of the cells, but did not specify how exactly the diameter was determined. We plan to perform a detailed microscopy study in combination with our method in the future to resolve these issues.

As for the refractive index, we are aware of only one study where the cytoplasmic refractive index of human lymphocytes was measured.[7] The index-matching method was used leading to a mean value of m_c equal to $1.3572 ± 0.0002$ (standard error of mean) for several normal donors, which is signifi-

cantly lower than values obtained in the current study. This is because our method determines the integral (effective) refractive index of the whole cytoplasm, including all granules and other inclusions, while index matching yields the value for the ground substance of the cytoplasm.

The fact that we use only a small part of LSPs measured with the SFC for sample characterization is due to the small confidence levels of the majority of the experimental LSPs, or, (approximately) equivalently, large standard deviations of model parameter estimates. As we discussed in Sec. 2.5, this is mostly due to model errors, i.e., the fact that real lymphocytes are not perfect coated spheres. To better understand these errors, we performed a limited set of DDA simulations. First, we tried to shift the nucleus inside the coated sphere model, but that showed no considerable effect on the structure of the LSP, except for scattering angles larger than 40 deg. Such LSPs are successfully processed, with the global optimization resulting in a confidence level above 0.95 and accurate estimation of the model parameters (data not shown). This is partly due to the large nucleus diameter used (D_n/D_c=0.9), which is why it may seem to contradict earlier simulations using smaller nucleus diameters, e.g., Ref. 47.

Second, we tested the enhanced model including nucleus inhomogeneity (see Sec. 3.2 and right part of Fig. 8). The estimated mean parameters of the T-cells of donor 6 were used in simulation of light scattering for the cell model (see corresponding column of Table 1): D_c=6.38 μm, D_n/D_c=0.903, m_c=1.3765, and average m_n=1.4476. Since now the nucleus consists of two domains, we chose for the inner spheroid the same refractive index as the cytoplasm (to maximize the contrast) and a larger refractive index (1.457) for the rest of the nucleus. Then the average (effective medium) refractive index of the nucleus equals the one specified before. The spheroid has axis ratios 1:2:2, its volume is 0.108 of the whole nuclear volume, its center coincides with the center of the cell, and the orientation of the symmetry axis with a respect to the light incidence direction θ_0 was varied from 0 to 90 deg with a step of 30 deg. Results of processing the simulated LSPs with the global optimization are shown in Fig. 10.

One can see that the nuclear inhomogeneity (with volume fraction of only 10%) significantly distorts the LSPs, resulting in large errors of parameter estimates. Therefore, the proposed nuclear inhomogeneity may be a significant part of optical model errors for lymphocytes. But, of course, more simulations are required to make any definite conclusions. On the other hand, the global optimization performs reliably on these distorted LSPs, i.e., the real values of the initial model are
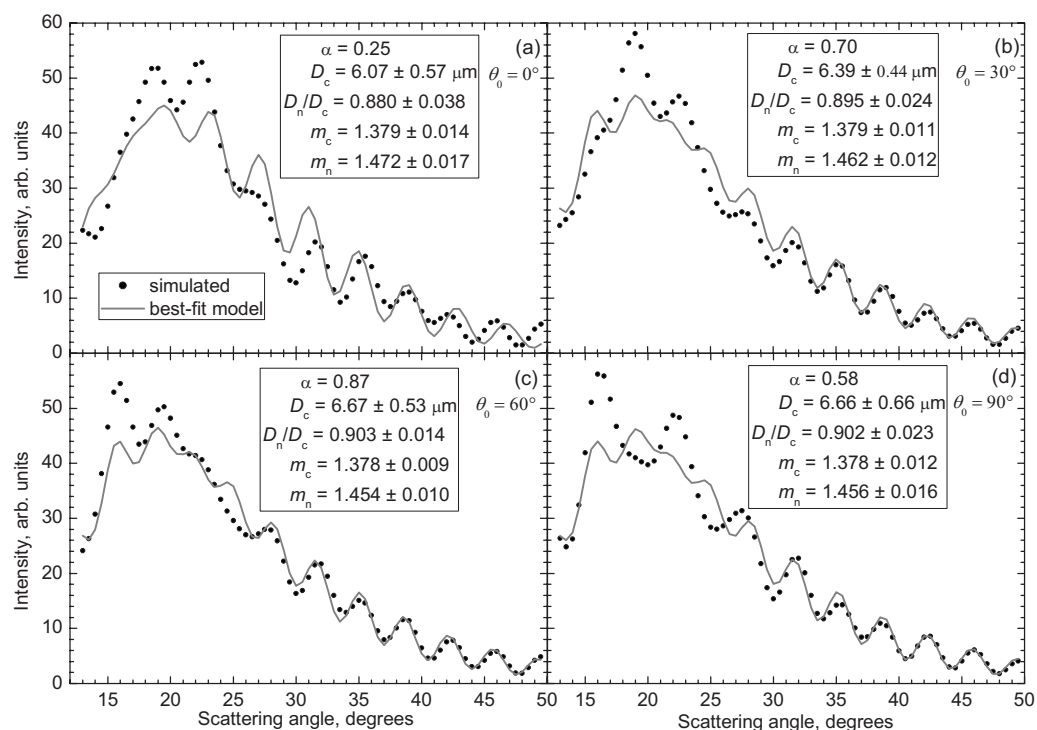
Fig. 10 Results of global optimization for four simulated LSPs corresponding to the enhanced optical model of a lymphocyte. Each graph shows simulated and best-fit weighted LSPs, and corresponds to different orientation of the oblate spheroid inside the nucleus. Estimates of the cell characteristics (expectation value±standard deviation) are also shown.

well inside the confidence intervals (although the latter may be large). From the obtained confidence levels, we can suggest that using the threshold $\alpha_0 = 0.8$ leaves only cells with a relatively homogeneous nucleus (but possibly shifted from the center of the cell). We may suggest that these cells are in G1-phase of a cell cycle.[48]

3.4 Comparison of Cellular Characteristics for T- and B-Cells

Comparing the results of the global optimization for characterization of T- and B-lymphocytes (Table 2), one can see that the main difference in T- and B-cell morphology is the mean cell size $\langle D_c \rangle$. Although the difference in $\langle D_c \rangle$ of about 5% is statistically significant, it is smaller than the estimated biological variability $\sigma(D_c)$ inside each sample. Hence, at present we cannot reliably classify a single lymphocyte as being T- or B-, using only its morphological characteristics determined from LSP. However, one may try to estimate the relative count of T- to B-lymphocytes in a sample, processing the distribution of all lymphocytes over morphological characteristics as a bimodal distribution (e.g., a sum of two multidimensional normal distributions). A similar method was proposed by Terstappen et al.[49] using the distribution of lymphocytes over the side scattering signal. However, further research is required to assess the accuracy of such relative count estimates.

Another way of looking at differences between T- and B-lymphocytes is studying average LSPs. First, we averaged 100 experimental LSPs from the samples of T- and B-lymphocytes for donor 6, resulting in Fig. 11(a). There is a difference in intensity for scattering angles from
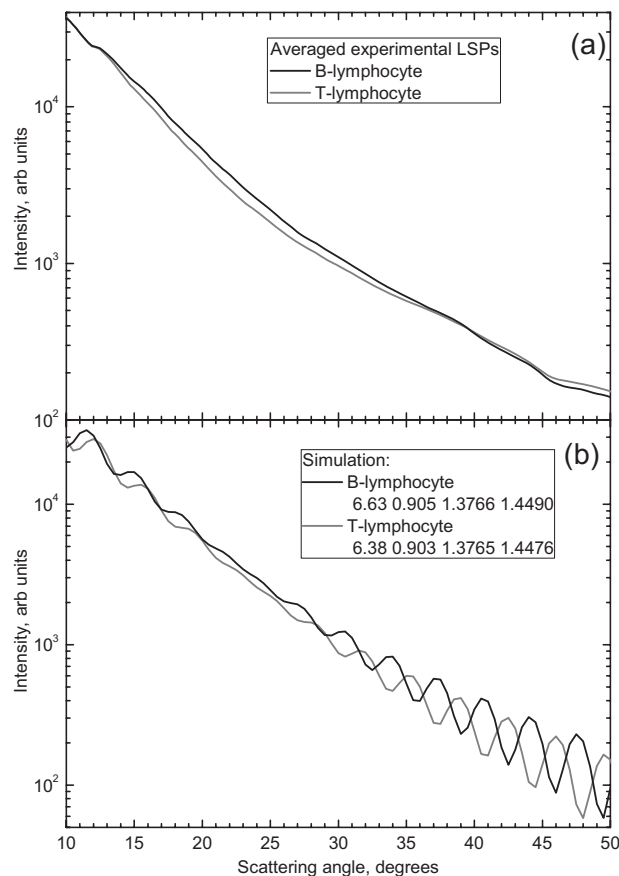

Fig. 11 The LSPs of T- and B-lymphocytes for donor 6 (in logarithmic scale): (a) experimental averaged over a sample; and (b) simulated using the estimates of the mean values of model characteristics over sample.

15 to 35 deg. However, this difference is much smaller than the natural variability of LSPs inside each sample (see Fig. 7). Second, we simulated LSPs of lymphocytes specified by estimates of the mean values of model characteristics, resulting in Fig. 11(b). The structure of these LSPs in the angular range from 20 to 27 deg is different from the rest of the interval, because it contains almost no oscillations. Moreover, in this range, the LSP of the average T-lymphocyte has smaller intensity than that of the average B-lymphocyte, which agrees with Fig. 11(a). This is explainable, since oscillations smooth out during averaging over the sample, while differences in monotonous parts of the LSP are more likely to persist. It will be interesting to identify which morphological characteristics are responsible for this angular interval in the LSP. But currently we can only conclude that the difference in mean diameter at least partly explains the difference in averaged LSPs.

We also note that B-cells are generally better fitted by the coated sphere model than T-cells. An example is presented in Fig. 12, showing that standard deviations of estimated D_c for donor 6 are on average smaller for B-lymphocytes. Results for other characteristics and donor 1 are similar (data not shown). We hypothesize that this fact can be caused by smaller deviation of the shape of B-lymphocytes from the coated sphere, in particular a relatively smaller inhomogeneity of the nucleus.

4 Conclusion

We describes a method for the solution of the inverse light-scattering problem for individual mononuclear cells. Our method is based on fitting experimental light-scattering patterns (LSPs) by a coated sphere model using the global optimization algorithm DIRECT. The deviation of real lymphocyte morphology from the model is considered a quasirandom error. This causes residuals of the best fit to be correlated, which is accounted for approximately by using a reduced number of degrees of freedom. Errors of parameter estimates are determined by Bayesian inference using the description of the sum of squares surface provided by the DIRECT algorithm. The distribution of model characteristics over sample (its mean and covariance matrix) is estimated, accounting for different reliability of parameter estimates for different particles.

We use this method to characterize lymphocytes of several donors, determining cell diameter, ratio of nucleus to cell diameters, nucleus, and cytoplasm refractive indices. The main difference in morphology of T- and B-lymphocytes is found to be the larger mean diameters of the latter. However, the difference is smaller than the biological variability of diameters for both T- and B-lymphocytes of a single donor.

We also perform preliminary simulations using a more complicated model derived from confocal images of real lymphocytes. The results suggest that deviations of real lymphocyte LSPs from the best-fit LSP of the coated sphere model may be due to nuclear inhomogeneity. Moreover, this inhomogeneity is probably slightly less pronounced for B- than for T-lymphocytes, resulting in generally smaller errors of parameter estimates of the former. However, much more detailed study is required to make any definite conclusion about the exact shape of nuclear inhomogeneity of lymphocytes and its effect on their LSPs. In particular, differentiating T- and
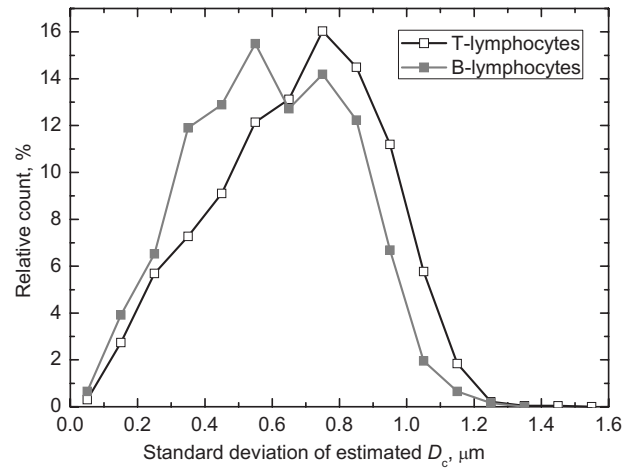

Fig. 12 Distribution of standard deviations of estimated cell diameter for samples of T- and B-lymphocytes of donor 6.

B-lymphocytes from light-scattering data clearly requires a more sophisticated lymphocyte model.

Currently, processing one LSP with the proposed method takes approximately 150 sec with a modern desktop PC (1.8 GHz). Up to five local minima are identified on the least-square surface, depending on a particular LSP. For now we concentrated on the robustness of the algorithm (reaching global minima and sufficiently detailed description of the least-square surface), and did not pursue its numerical efficiency. Two orders of magnitude in the decrease of processing time is required to make incorporation of this method into a routine blood cell analysis feasible. This is an important goal for future research.

References

1. I. M. Roitt, *Roitt's Essential Immunology*, 9th ed., Blackwell Science, Oxford (1997).
2. *Flow Cytometry Protocols*, T. S. Hawley and R. G. Hawley, Eds., Humana Press, Totowa, NJ (2004).
3. H. D. Alexander, G. M. Markey, R. L. Nolan, and T. C. M. Morris, "Cell sizing in chronic lymphoproliferative disorders: an aid to differential diagnosis," *J. Clin. Pathol.* **45**, 875–879 (1992).
4. S. Galimberti, R. Riccioni, A. Azzara, R. Testi, R. Fazzi, C. Testi, and M. Petrini, "Unusual morphology in a case of large granular cell leukemia," *Ann. Hematol.* **80**(12), 755–757 (2001).
5. M. Nerenberg, I. Kariv, P. McNeeley, P. Marchand, S. Sur, J. Diver, S. Riccitelli, J. Nieva, and A. Saven, "Use of optophoresis as an in vitro predictor of cell response to chemotherapy for chronic lymphocytic leukemia," *Leuk. Lymphoma* **47**(10), 2194–202 (2006).
6. A. Zipursky, E. Bow, R. S. Seshadri, and E. J. Brown, "Leukocyte

density and volume in normal subjects and in patients with acute lymphoblastic leukemia," *Blood* **48**(3), 361–371 (1976).

7. W. K. Metcalf, N. F. Metcalf, and R. N. Gould, "Lymphocyte cytoplasmic refractive index (LCRI)," *Antibiot Chemother.* **22**, 149–154 (1978).

8. A. Giacomini, P. Legovini, F. Antico, G. Gessoni, S. Valverde, M. M. Salvadego, and F. Manoni, "Evaluation of platelet analysis on the ADVIA 120 hematology system," *Lab. Hematol.* **7**, 180–185 (2001).

9. T. Ghys, R. Malfait, and J. van den Bossche, "Performance evaluation of the Sysmex XS-1000i automated haematology analyser," *Intl. J. Lab. Hematol.* **31**, 560–566 (2009).

10. T. Lehto and P. Hedberg, "Performance evaluation of Abbott CELL-DYN Ruby for routine use," *Intl. J. Lab. Hematol.* **30**, 400–407 (2008).

11. L. Peng, L. Bai, L. Nie, Z. Wu, and C. Yan, "Performance evaluation of BC-3200 hematology analyzer in a university hospital," *Intl. J. Lab. Hematol.* **30**, 205–213 (2008).

12. K. Guerti, F. Vertessen, L. Daniels, and M. van der Planken, "Performance evaluation of the PENTRA 60C+ automated hematology analyzer and comparison with the ADVIA 2120," *Intl. J. Lab. Hematol.* **31**, 132–141 (2009).

13. V. P. Maltsev and K. A. Semyanov, *Characterisation of Bio-Particles from Light Scattering, Inverse and Ill-Posed Problems Series*, VSP, Utrecht (2004).

14. E. Hirst and P. H. Kaye, "Experimental and theoretical light scattering profiles from spherical and nonspherical particles," *J. Geophys. Res., [Atmos.]* **101**, 19231–19235 (1996).

15. R. S. Brock, X. H. Hu, D. A. Weidner, J. R. Mourant, and J. Q. Lu, "Effect of detailed cell structure on light scattering distribution: FDTD study of a B-cell with 3D structure constructed from confocal images," *J. Quant. Spectrosc. Radiat. Transf.* **102**, 25–36 (2006).

16. I. K. Ludlow and J. Everitt, "Application of Gegenbauer analysis to light-scattering from spheres-theory," *Phys. Rev. E* **51**, 2516–2526 (1995).

17. S. L. Min, and A. Gomez, "High-resolution size measurement of single spherical particles with a fast Fourier transform of the angular scattering intensity," *Appl. Opt.* **35**, 4919–4926 (1996).

18. K. A. Semyanov, P. A. Tarasov, A. E. Zharinov, A. V. Chernyshev, A. G. Hoekstra, and V. P. Maltsev, "Single-particle sizing from light scattering by spectral decomposition," *Appl. Opt.* **43**, 5110–5115 (2004).

19. Z. Ulanowski, Z. N. Wang, P. H. Kaye, and I. K. Ludlow, "Application of neural networks to the inverse light scattering problem for spheres," *Appl. Opt.* **37**, 4027–4033 (1998).

20. V. V. Berdnik, K. Gilev, A. N. Shvalov, V. P. Maltsev, and V. A. Loiko, "Characterization of spherical particles using high-order neural networks and scanning flow cytometry," *J. Quant. Spectrosc. Radiat. Transf.* **102**, 62–72 (2006).

21. M. A. Yurkin, K. A. Semyanov, P. A. Tarasov, A. V. Chernyshev, A. G. Hoekstra, and V. P. Maltsev, "Experimental and theoretical study of light scattering by individual mature red blood cells by use of scanning flow cytometry and a discrete dipole approximation," *Appl. Opt.* **44**, 5249–5256 (2005).

22. J. Neukammer, C. Gohlke, A. Hope, T. Wessel, and H. Rinneberg, "Angular distribution of light scattered by single biological cells and oriented particle agglomerates," *Appl. Opt.* **42**(31), 6388–6397 (2003).

23. A. E. Zharinov, P. A. Tarasov, A. N. Shvalov, K. A. Semyanov, D. R. van Bockstaele, and V. P. Maltsev, "A study of light scattering of mononuclear blood cells with scanning flow cytometry," *J. Quant. Spectrosc. Radiat. Transf.* **102**, 121–128 (2006).

24. C. F. Bohren and D. R. Huffman, *Absorption and Scattering of Light by Small Particles*, Wiley, New York (1983).

25. D. R. Jones, C. D. Perttunen, and B. E. Stuckman, "Lipschitzian optimization without the Lipschitz constant," *J. Optim. Theory Appl.* **79**, 157–181 (1993).

26. M. G. Ormerod, "Preparing suspensions of single cells," in *Flow Cytometry: A Practical Approach*, 3rd ed., pp. 35–45, Oxford University Press, Oxford (2000).

27. V. P. Maltsev, "Scanning flow cytometry for individual particle analysis," *Rev. Sci. Instrum.* **71**, 243–255 (2000).

28. M. A. Yurkin and A. G. Hoekstra, "The discrete dipole approximation: an overview and recent developments," *J. Quant. Spectrosc. Radiat. Transf.* **106**, 558–589 (2007).

29. M. A. Yurkin, V. P. Maltsev, and A. G. Hoekstra, "The discrete dipole approximation for simulation of light scattering by particles much larger than the wavelength," *J. Quant. Spectrosc. Radiat. Transf.* **106**, 546–557 (2007).

30. "ADDA—light scattering simulator using the discrete dipole approximation," see http://code.google.com/p/a-dda/ (2009).

31. "Description of the national compute cluster Lisa," see https://subtrac.sara.nl/userdoc/wiki/lisa/description (2009).

32. V. A. Loiko, G. I. Ruban, O. A. Gritsai, A. D. Gruzdev, S. M. Kosmacheva, N. V. Goncharova, and A. A. Miskevich, "Morphometric model of lymphocyte as applied to scanning flow cytometry," *J. Quant. Spectrosc. Radiat. Transf.* **102**, 73–84 (2006).

33. G. Ruban, S. Kosmacheva, N. Goncharova, D. van Bockstaele, and V. Loiko, "Investigation of morphometric parameters for granulocytes and lymphocytes as applied to a solution of direct and inverse light-scattering problems," *J. Biomed. Opt.* **12**, 044017 (2007).

34. A. M. Dunn, "Modeling of light scattering from inhomogeneous biological cells," in *Optics of Biological Particles*, A. G. Hoekstra, V. P. Maltsev, and G. Videen, Eds., pp.19–29, Springer, Dordrecht, Germany (2006).

35. G. A. F. Seber and C. J. Wild, *Nonlinear Regression*, Wiley-Interscience, Hoboken, NJ (2003).

36. D. M. Bates and D. G. Watts, *Nonlinear Regression Analysis and Its Applications*, Wiley, New York (1988).

37. S. V. Aleinik, "Approximate probability density of the sum of squares of correlated normal variates," *Radiotekhnika (Moscow)* **1**, 53–55 (1999) [in Russian].

38. W. A. Fuller, "Prediction of true values for the measurement error model," in *Statistical Analysis of Measurement Error Models and Applications*, P. Brown and W. A. Fuller, Eds., pp. 41–58, American Mathematical Society, Providence, RI (1990).

39. D. Y. Orlova, M. A. Yurkin, A. G. Hoekstra, and V. P. Maltsev, "Light scattering by neutrophils: model, simulation, and experiment," *J. Biomed. Opt.* **13**, 054057 (2008).

40. J. T. Soini, A. V. Chernyshev, P. E. Hanninen, E. Soini, and V. P. Maltsev, "A new design of the flow cuvette and optical set-up for the scanning flow cytometer," *Cytometry* **31**, 78–84 (1998).

41. F. Shido, K. Kobayashi, and N. Yamanaka, "Cell-size distribution of human tonsillar lymphocytes," *Arch. Otorhinolaryngol. Suppl.* **239**, 211–218 (1984).

42. R. K. Cheung, S. Grinstein, and E. W. Gelfand, "Volume regulation by human lymphocytes. Identification of differences between the two major lymphocyte subpopulations," *J. Clin. Invest.* **70**, 632–638 (1982).

43. S. Grinstein and J. D. Smith, "Calcium-independent cell volume regulation in human lymphocytes. Inhibition by charybdotoxin," *J. Gen. Physiol.* **95**, 97–120 (1990).

44. M. Konwinski and T. Kozlowski, "Morphometric study of normal and phytohemagglutinin-stimulated lymphocytes," *Cell Tissue Res.* **129**, 500–507 (1972).

45. S. Majstoravich, J. Zhang, S. Nicholson-Dykstra, S. Linder, W. Friedrich, K. A. Siminovitch, and H. N. Higgs, "Lymphocyte microvilli are dynamic, actin-dependent structures that do not require Wiskott-Aldrich syndrome protein (WASp) for their morphology," *Blood* **104**, 1396–1403 (2004).

46. M. Wehling, S. Kuhls, and D. Armanini, "Volume regulation of human lymphocytes by aldosterone in isotonic media," *Am. J. Physiol. Endocrinol. Metab.* **257**, E170–E174 (1989).

47. A. Hoekstra, M. Grimminck, and P. Sloot, "Large scale simulations of elastic light scattering by a fast discrete dipole approximation," *Int. J. Mod. Phys. C* **9**, 87–102 (1998).

48. A. Murray and T. Hunt, *The Cell Cycle*, Oxford University Press, Oxford (1993).

49. L. W. Terstappen, B. G. De Grooth, C. H. Ten Napel, W. van Berkel, and J. Greve, "Discrimination of human cytotoxic lymphocytes from regulatory and B-lymphocytes by orthogonal light scattering," *J. Immunol. Methods* **95**, 211–216 (1986).